Title

Local atomic configurations in mechanically alloyed amorphous (FeCoNi)70Ti10B20 powders

Authors

Kalkan, Bora

Simsek, Tuncay

Avar, Baris

Publication Date

2023-10-01

DOI

10.1016/j.jallcom.2023.170667

Local Atomic Configurations in Mechanically Alloyed Amorphous $(FeCoNi)_{70}Ti_{10}B_{20}$ Powders

Bora Kalkan*[1,2], Tuncay Simsek[3] and Baris Avar[4]

[1]*Earth and Planetary Sciences Department, University of California, Santa Cruz, CA 95064, USA*

[2]*Advanced Light Source, Lawrence Berkeley National Laboratory, Berkeley, CA 94720, USA*

[3]*Department of Mechanical and Metal Technologies, Kırıkkale University, Kırıkkale 71450, Turkey*

[4]*Department of Metallurgical and Materials Engineering, Zonguldak Bülent Ecevit University, Zonguldak 67100, Turkey*

Abstract

The atomic structure of amorphous $(FeCoNi)_{70}Ti_{10}B_{20}$ alloy synthesized by mechanical alloying was investigated using high energy synchrotron X-ray diffraction and inverse Monte Carlo simulations of pair distribution functions. Empirical potential structure refinement indicates a chemical short-range order at the length scales of 2.1-2.5 Å via local atomic arrangements forming deformed bcc-like clusters. The structural model obtained was described by bond lengths, coordination numbers, and bond angle distribution functions determined for the first neighbor atoms by x-ray scattering supplemented with 3D Monte Carlo simulations.

Keywords:
Amorphous alloy; Short range order: X-ray diffraction: Inverse Monte Carlo Simulations: PDF analysis

Highlights:

- Chemically ordering in the short range is consistent with the experimental data.
- Deformed bcc-like clusters form the local atomic arrangements.
- A clear tendency for clustering around B and Ti atoms, not observed for Fe, Co, and Ni.
- Structural motifs are investigated in detail.

1. Introduction

Transition metal-based amorphous alloys had a great interest in the last decade due to their unique mechanical (ultrahigh strength, wear resistance) [1-4] and physical properties (soft magnetic) [5-7]. Especially Fe-based amorphous alloys have been frequently examined due to their low coercive force, high saturation magnetization, and high permeability, which make these materials potential candidates for many technological applications [8] like magnetic recording media and magnetic fluids. The addition of some late transition metals (Co, Ni, Cu) into a Fe-based system has been studied to increase soft magnetic properties [9-11]. The combination of this system with early transition metals (Ti, Zr, Nb) extended this family [12, 13]. It was well studied that the addition of some metalloid elements (B, C, and Si) improved the disordered phase formation ability extensively [14-17].

Several ways have been used to synthesize these alloys, such as rapid quenching and mechanical alloying (MA). Among them, mechanical allying is the most widely used due to its simplicity, low cost, and capability of producing a high amount of material [18]. In our recent research, amorphous $(FeCoNi)_{70}Ti_{10}B_{20}$ was synthesized successfully through MA, and phase stability of the amorphous structure has been investigated under extreme conditions, such as high pressure and temperature [19].

Even though there are various attempts focused on the synthesis and understanding of the physical and mechanical properties of these materials in the literature, studies targeting the structural properties are very rare [20]. Indeed, their physical properties are mainly determined by the structure, which can be described by local atomic configurations in the short and medium range. The most common reason for the lack of these studies is that systems consist of many components which depend on each other. On the one hand, interactions between components

complicate structural modelling and related pair correlations. That's why it is not surprising that many scholars have studied synthesis routes and mechanical and physical properties of these multi-component systems. Here, we present a detailed structural investigation of the short- and medium-range ordering in amorphous $(FeCoNi)_{70}Ti_{10}B_{20}$ at ambient conditions using synchrotron x-ray scattering in combination with Empirical Potential Structure Refinement (EPSR) simulations based on Monte-Carlo modelling.

2. Experimental

The initial mixture has been prepared from elemental powders of Fe (Aldrich, 99.9%), Co (Aldrich, 99.9%), Ni (Aldrich, 99.9%), Ti (Aldrich, 99.9%), and B (Aldrich, 99.9%), with the nominal composition of $(FeCoNi)_{70}Ti_{10}B_{20}$. The alloying process was carried out using a planetary-type ball mill at room temperature. The amorphous phase has been remarkably enhanced after 30 h ball milling which was stopped at the end of 50 h. The amorphous nature of the alloyed sample was characterized by the angle dispersive X-ray diffraction (XRD) technique. The full details of the ball milling process have been reported in our earlier study [19].

The XRD measurements on the synthesized samples sealed in 0.7 mm quartz capillaries were performed on the Beamline 12.2.2 at Advanced Light Source, Lawrence Berkeley National Laboratory [21]. The incident beam energy used was 30 keV (yielding the wavelength of λ=0.4133 Å) and the monochromatic beam was focused to a size of 30 µm x 30 µm at the sample position. Diffracted X-ray intensities were collected on a Pilatus3 S 1M fast detector at a distance of 238.6 mm calibrated using a CeO_2 standard. This geometry allowed diffraction data to be collected up to maximum scattering vector magnitude Q = 7.2 $Å^{-1}$. A typical exposure time of 120 s was selected for data collection. The diffraction images were radially integrated using the program DIOPTAS [22].

3. EPSR Monte Carlo Simulations

The inverse Monte Carlo simulation technique coded as Empirical Potential Structure Refinement (EPSR) was used to determine the atomic structure of amorphous $(FeCoNi)_{70}Ti_{10}B_{20}$ alloy [23]. A Monte Carlo computer simulation of the system $(FeCoNi)_{70}Ti_{10}B_{20}$ was created using 999 atoms in total within a cubic box with a volume constrained by the determined mass density (Table 1). Atoms interacted via a Lennard-Jones (12-6) potential [24]. The parameters defining the interatomic pair potentials used in the structure refinements, taken from Ref. [25-29], are listed in Table 1. Minimum approach distances, listed in Table 2 for related atom pairs, are calculated using the atomic radii of each atom and served as constraints in carrying out Monte Carlo simulations.

Simulations are run based on the strategy presented as follows: A first convergence is reached (in the first ~7200 iterations) for a fixed temperature of 1000 K without empirical potential structure refinement. Then, the atomistic configuration is relaxed more by decreasing the temperature to 298 K, and stays in equilibrium up to 18650 iterations. In the next stage, the refinement loop is started by introducing the empirical potential. Our fit to experimental total structure factor, S(Q) yields chi-square value around $\chi^2 = 0.0017$, with a better convergence in ~19500 iterations. The last atomic configuration and best fits were achieved after ~43034 iterations of the EPSR steps (Figure 1).

4. Results and Discussion

4.1. Data reduction to get S(Q) from raw XRD patterns

Details of the process used to obtain the structure factor from the high-energy XRD pattern are shown in Figure 2. Before taking into account the standard intensity corrections, such as background subtraction, absorption correction, multiple-scattering correction, and incoherent

Compton scattering, a proper correction for oblique incidence (OI) of the beam on the detector sensor layer (1 mm thick Silicon for Pilatus3 S 1M) has been applied on both raw sample data and the background collected from the empty capillary (see Figure 2). A correction factor (*K*) for oblique incidence (Equation 1) which is relative to normal incidence direction was used and the corrected intensities were determined using the equation of $I\ (OI\ corrected) = I_{observed} / K$.

$$K = \frac{\left[1-e^{-\frac{\mu d}{cos\alpha}}\right]}{\left[1-e^{-\mu d}\right]} \quad (1)$$

In Equation 1, d is the thickness of the detector layer, equals 1mm, and μ denotes the fraction of the intensity loss per millimeter (linear absorption coefficient) and equals 0.3346 mm^{-1} at 30 keV (obtained from the online database of the National Institute of Standards and Technology [30]). The angle between the diffracted beam and the normal to the detector sensor layer surface is represented with α. Values of K derived with Equation 1 are shown as a function of Q in Figure 2 as an inset.

Correction of container (capillary) scattering has been done as follows. The sample scattering intensity, $I_S(Q)$ can be expressed in the form of Equation 2 [31]:

$$I_S(Q) = I_{S,C}(Q) - \left(\frac{A_{S,C}\,(Q,E)}{A_C\,(Q,E)}\right) I_C(Q) \quad (2)$$

where: $A_{S,C}\,(Q)$ and $A_C\,(Q)$ are the geometrical absorption terms [32], $I_C(Q)$ is the intensity scattered by capillary, and $I_{S,C}(Q)$ is the intensity from the sample and the capillary. For the transmission geometry, the ratio of $A_{S,C}\,(Q)$ and $A_C\,(Q)$ can be expressed as of Equation 3[32]:

$$\frac{A_{S,C}\,(Q,E)}{A_C\,(Q,E)} = e^{-\frac{\mu_S\,(E)\,t_S}{cos\,x}} \quad (3)$$

where: x is the angle between sample surface normal and incident beam, $\mu_S\,(E)$ is the linear absorption coefficient of the sample, and t_S is thickness of the sample. It can be simplified that

cosx ≈1 since x~0 in the transmission geometry. The term of $e^{-\mu_S(E)\,t_S}$ can be written in terms of the intensities of X-rays transmitted through the sample and capillary ($I_{S,C}^{transmitted}$ and $I_C^{transmitted}$) measured from two separate experiments, the first with capillary filled with sample and the second with empty capillary (see Equation 4).

$$\frac{I_{S,C}^{transmitted}}{I_C^{transmitted}} = e^{-\frac{\mu_S(E)\,t_S}{\cos x}} \quad (4)$$

The integrated patterns of the x-ray scattering for $(FeCoNi)_{70}Ti_{10}B_{20}$ after background correction is shown in Figure 2 along with the empty-capillary background.

The detector dead-time effect was corrected using the method reported in Ref. [33]. The multiple scattering intensity, considered only for the double scattering process since it represents the major part of the multiple scattering, was computed following the method reported by Warren and Mozzi [34]. The intensity difference due to the multiple scattering, dead-time corrections and sample absorption are small, and not presented in Figure 2. Partial polarization of scattered beam by atoms will have an effect on the measured scattered intensity as a function of scattering angle and can be corrected using the Equation 5:

$$P(2\theta) = \frac{(1+x\cos^2 2\theta)}{(1+y)} \quad (5)$$

where x = y =cos $2\alpha_c$ (since the monochromator is located in the incident beam side at Beamline 12.2.2 [21]) , and α_c is the Bragg angle of the monochromator crystal (equals to 4.2° for Si(111) monochromator crystal at Beamline 12.2.2 optics). Polarization corrected intensity is shown in Figure 2. By introducing a normalization factor *N* (Equation 6), the total scattering from the sample $I^{corrected}(Q)$ can be expressed in atomic units in terms of coherent scattering $I^{coherent}(Q)$, incoherent scattering $I^{incoherent}(Q)$:

$$N\,I^{corrected}(Q) = I^{coherent}(Q) + I^{incoherent}(Q) \quad (6)$$

$I^{corrected}(Q)$ corresponds to the data after corrections for oblique incidence, background, dead-time, multiple scattering, polarization, and absorption. The computing of normalization factor N and incoherent scattering (Compton scattering) contribution, using the atomic scattering factors, were done based on the methodology reported in our previous studies [35, 36].

The coherent x-ray scattering intensity, $I^{coherent}(Q)$ for a disordered system is expressed by the following in terms of the Faber-Ziman (FZ) notation [37],

$$I^{coherent}(Q) = (\langle f^2 \rangle - \langle f \rangle^2) + \langle f \rangle^2 S(Q) \quad (7)$$

In Equation 7, the $\langle f^2 \rangle - \langle f \rangle^2$ term is attributed to the intensity arising only from the difference in the atomic scattering factors of the constituent atoms. The square of the mean scattering factor $\langle f \rangle^2$ and the mean square average of the scattering factor $\langle f^2 \rangle$ were determined using the atomic fractions [38]. A typical example of the $I^{coherent}(Q)$ intensities normalized to $\langle f \rangle^2$ is shown in Figure 2 as inset.

4.2. Evolution of the structure factor S(Q)

The experimentally determined X-ray total structure factor for amorphous $(FeCoNi)_{70}Ti_{10}B_{20}$ is compared with the one calculated from EPSR simulations in Figure 3a. The S(Q) curve is characterized by an intense primary peak at 3.1 $Å^{-1}$ indicating chemical short range order at length scales of about 2.03 Å, and a secondary peak at about 5.2 $Å^{-1}$ that can be attributed topological order. A more intense primary peak in the S(Q) indicates that chemical ordering dominates, while the secondary peak exhibits a small contribution of topological order in short range length scale.

Total structure factor S(Q) is written as weighted sum of the partial structure factors (PSFs) S_{ij}(Q) in Faber-Ziman formalism [37] (Supporting information). The weighting factors and

weighted PSFs for atom pairs calculated from our EPSR simulations by direct inversion of the total $S(Q)$ as described in ref [23], are shown in Figures S1 and S2 (Supporting information). The contributions of PSFs can be discussed in terms of the three main groups: the first is the group of S_{FeCo}(Q), S_{NiCo}(Q) and S_{FeNi}(Q) which contributes about (15-19)%; and the second is S_{NiNi}(Q), S_{CoCo}(Q), S_{FeFe}(Q), S_{NiTi}(Q), S_{CoTi}(Q) and S_{FeTi}(Q) contributing around (7-10)%; and the last group of S_{NiB}(Q), S_{CoB}(Q), S_{FeB}(Q), S_{TiTi}(Q), S_{TiB}(Q) and S_{BB}(Q) at the contribution level of (0.5-3)%. The third group of PSFs has larger statistical noise compared to the others due to its small contribution to total S(Q) and the smaller relative fraction of Ti and B atoms in the $(FeCoNi)_{70}Ti_{10}B_{20}$ stoichiometry. The intense first group halos indicate high population of Fe-Co, Ni-Co, and Fe-Ni correlations at the length scale of the first neighborhood.

4.3. Atomic configuration

Figure 4 shows the representative three-dimensional (3D) plot of atomic-scale structural models of $(FeCoNi)_{70}Ti_{10}B_{20}$ obtained from EPSR simulations. It can be seen that the distribution of atoms is not homogeneous with more and less dense regions. For instance, a clear tendency for clustering is observed in the B-rich regions (Figure 5h, 5i, 5j, 5k, 5l). At a glance, a slight tendency for phase separation or clustering is also observed for Ti atoms mostly linked to either Ti or B atoms (Figure 5l). Fe-Ti (Figure 5e), Co-Ti (Figure 5f), and Ni-Ti (Figure 5g) correlations are not as random as Fe-Fe (Figure 5a), Fe-Co (Figure 5b), Fe-Ni (Figure 5c), and Co-Ni (Figure 5d) correlations. These results are in good agreement with Ref. [39-41], where it is presented that the amorphous structure contains dense packed and less dense packed atomic clusters. To confirm this, a pair distribution function analysis was used as a powerful tool.

4.4. Structure analysis in real space

From the total structure factor S(Q) by Fourier transformation according to Equation 8 the total reduced atomic pair distribution function G(r) is obtained:

$$G(r) = 4\pi r\rho_0[g(r) - 1] = \frac{2}{\pi}\int_0^\infty Q\,[S(Q) - 1]\sin(Qr)\,.\,dQ \qquad (8)$$

The EPSR-simulated G(r) of amorphous $(FeCoNi)_{70}Ti_{10}B_{20}$, as obtained from Fourier transformation of the corresponding $S(Q)$ pattern, is shown in Figure 3b. As $r \rightarrow 0$ $G(r)$ behaves like $-4\pi r\rho_0$, which is a straight line going through zero with a slope that is proportional to the average number density of the material. In Figure 3b, the slope was calculated for amorphous $(FeCoNi)_{70}Ti_{10}B_{20}$ at ambient conditions and yields an atomic number density of 0.0975 (± 0.026) atoms/Å^3 at room temperature and ambient pressure. Large oscillations below ~2.0 Å in G(r) indicate Fourier transform truncation caused by the finite range of Q measured. The G(r) has a strong peak at 2.5 Å manifested by short-range order in the structure. The second and third peaks located at ~4.4 Å and 5.0 Å are usually attributed to an interatomic distance characterizing group of atoms which can be considered as the signature of chemical short-range ordering (CSRO) in the amorphous structure [42]. The atomistic origin of G(r) can be quite complex and G(r) peaks can be composed of many sub-peaks, which can be identified with knowledge of the partial pair distribution functions (PDFs) (depicted in Figure 6).

The average interatomic distance corresponding to the first neighbors, R can be estimated from the position of the first peak in S(Q) located at 3.1 Å^{-1} using the Ehrenfest relation [43, 44] shown in Equation 9.

$$R = \frac{\lambda}{E\,sin\theta} \qquad (9)$$

In Equation 9, λ denotes the wavelength of the x-ray used, θ is the position of the first diffraction peak and E is the structure-dependent constant which can be taken as 1.627 [43, 44]. As a result, R-value of 2.47 Å is calculated as the average interatomic distance corresponding to the first neighborhood. Figure 6 (and Figure S3, Supporting information). shows that the first peak in the G(r) has contributions from all the correlations in the nearest-neighbor distance of (2.16-2.66) Å (see Table 2). Here, we also present and discuss the differences in the nearest-neighbor distances appearing during the simulations before and after introducing the empirical potential (EP). The partial PDFs distances before and after the introduction of the empirical potential are quite the same (Table 2). This reflects the fidelity of the Lennard-Jones terms used in modelling.

4.5. Local coordination numbers and bond-angle distributions

The coordination numbers of the nearest neighbor correlations calculated from the first peak area in the partial PDFs of amorphous $(FeCoNi)_{70}Ti_{10}B_{20}$ and total coordination numbers are listed in Table 2. The total coordination numbers of Fe, Co, and Ni are approximately equal (slightly above 13). In addition, the Fe-Co, Co-Ni, and Fe-Ni interatomic distances are quite the same, 2.49 Å, 2.52 Å, and 2.53 Å, respectively. These results indicate that Fe, Co and Ni atoms are randomly distributed in the alloy and play equivalent roles on local order formed by very similar-sized spheres indicates. This is supported by the similarity of Co-Ni-Ni, Fe-Ni-Ni, Fe-Co-Ni, Ni-Ni-Ni, Co-Ni-Co, Co-Co-Co, Ni-Fe-Ni, Co-Fe-Co, and Fe-Fe-Fe bond-angle distributions shown in Figure 7. What is important, the Fe/Co/Ni-centered clusters with the nearest coordination of slightly above 13 could be related to the atomic structure of α-Fe solid [19], which shows a body-centered cubic structure with a coordination number of 14 up to length scales of about 2.9 Å [45]. This is also supported by the results reported in our previous study showing phase analysis upon ball milling [19] and the existence of the α-Fe solid solution in the

samples ball milled in 0-10 h of milling. This fact means that in the amorphous $(FeCoNi)_{70}Ti_{10}B_{20}$ alloy, local atomic arrangements forming deformed bcc-like clusters are enriched, as observed in $Fe_{80}B_{20}$ amorphous alloy [46].

The results of the EPSR-simulated structure yield that the nearest-neighbor coordination numbers n_{FeFe}, n_{FeNi}, n_{FeCo}, n_{NiNi}, $n_{NiCo,}$ and n_{CoCo} are found to be around ~ 4 (or slightly lower than 4) indicating 4-fold coordination around Fe, Ni, Co atoms. On the other hand, n_{FeB}, n_{FeTi}, n_{NiB}, n_{NiTi}, n_{CoB}, and n_{CoTi} yield that Fe, Ni, and Co atoms are coordinated to one B and Ti atoms. Around B- atoms, the total nearest-neighbor coordination number is around ~11, which is the sum of n_{BB} ~ 5.7, n_{BTi} ~ 1.9, n_{BCo}~1.2, n_{BNi}~1.2, and n_{BFe}~1.2. The n_{BB} ~ 5.7 can be related to distorted octahedron or triangular atomic arrangements of B atoms around the center B atom. The clusters with n_{TiTi} ~ 4.1 coordination number could be related to Bernal's double tetrahedrons which are composed of two tetrahedral sharing the faces [47] and cannot lead to three-dimensional repeat structures. This may indeed provide the explanation for the inhomogeneous distribution of Ti-atoms with more or less dense regions.

In the present work, some typical polyhedrons taken from the equilibrium structure of amorphous $(FeCoNi)_{70}Ti_{10}B_{20}$ alloy are displayed in Figure 8. The maxims at about 109-115° in the Ni-Ni-Ni, Co-Ni-Co, Co-Co-Co, Ni-Fe-Ni, Co-Fe-Co, and Fe-Fe-Fe bond-angle distributions are very close to the tetrahedral angle of 109.5° in a perfect tetrahedron and indicates that there is close to 4-fold Fe, Co, and Ni coordination around Fe (Figure 8a, 8b, 8c, 8d), Co coordination around Co (Figure 8i), Co coordination around Ni (Figure 8j), and Ni coordination around Ni (Figure 8m). These bond angle distributions are also characterized by a sharp peak at about 58-62° that can be attributed to inter-tetrahedral triangular surfaces (Figure 8a, 8c, 8d, 8i, 8l, 8m, 8u). The sharp peak at about 58-62° in Co-Ni-Ni (Figure 8j, 8k), Fe-Ni-Ni (Figure 8s, 8r) and Fe-

Co-Ni (Figure 8p) distributions correspond to distorted triangular surfaces in related polyhedrons. The broad peak ranging from 100° to 125° in Fe-Ni-Ni can be related with inter polyhedral unit correlations and characterize the linkage between them (Figure 8t). The double tetrahedrons shown in Figure 8f are characterized by a sharp 56° intra-tetrahedral Ti-Ti-Ti bond angle. The broad peaks ranging from 30° to 70° (centered around 51° and 56°) in B-B-B and B-Ti-B bond angle distributions are captured in Figure 8e-8h representing highly distorted octahedron or triangular B-B and B-Ti correlations. Less dominant Fe-B-Ti distributions are consistent with the scenario where B and Ti atoms show a non-homogenous distribution and a clear tendency for clustering via B-B and B-Ti bonding, and rarely linkage to Fe atoms via Fe-B-Ti bridges (Figure 8q). Figures 8n and 8o indicate that Ni atoms in the Fe-Ni polyhedral units have been occasionally replaced with B and Ti atoms.

5. Conclusions

The combined X-ray scattering and EPSR simulation results (three-dimensional atomic model) presented in this study strongly reveal a nonhomogeneous distribution of atoms in amorphous $(FeCoNi)_{70}Ti_{10}B_{20}$ powders produced by mechanical alloying. Equilibrium structures taken from EPSR simulations reveal that clustering is more favorable in B- and Ti-rich regions via B-B, B-Ti, and Ti-Ti bonds. Several examples of representative Fe-, Ni- and Co- centered clusters taken from modeled amorphous structure indicated the nearest coordination close to 14 which reminiscences post α-Fe like atomic arrangement in short-range order. The results suggest that distorted polyhedral units with triangular faces (double tetrahedrons and octahedrons) are present in the atomic structure of the amorphous $(FeCoNi)_{70}Ti_{10}B_{20}$ alloy. The presented results in fact provide benchmarks for the molecular dynamic simulations targeting the understanding of the structure-property relationship in similar multicomponent amorphous alloys.

CRediT authorship contribution statement

Bora Kalkan: Conceptualization, Methodology, Writing - original draft, Modelling, Data analysis, Data collection. **Tuncay Simsek**: Material Synthesis, Writing - review & editing, Resources. **Baris Avar**: Material Synthesis, Writing - review & editing, Resources.

Declaration of Competing Interest

The authors declare that they have no known competing financial interests or personal relationships that could have appeared to influence the work reported in this paper.

Acknowledgement

This research used resources of the Advanced Light Source, a U.S. DOE Office of Science User Facility under contract no. DE-AC02-05CH11231, and was partially supported by COMPRES, the Consortium for Materials Properties Research in Earth Sciences under NSF Cooperative Agreement EAR 1606856.

References

[1]. X. Zhang, L. Lai, S. Xiao, H. Zhang, F. Zhang, N. Li, S. Guo, Effect of W on the Thermal Stability, Mechanical Properties and Corrosion Resistance of Fe-Based Bulk Metallic Glass, Intermetallics 143 (2022) 107485.

[2]. A. Inoue, B. L. Shen, C. T. Chang, Super-High Strength of over 4000 MPa for Fe-Based Bulk Glassy Alloys in $[(Fe_{1-x}Co_x)_{0.75}B_{0.2}Si_{0.05}]_{96}Nb_4$ System, Acta Mater. 52 (2004) 4093–4099.

[3]. S. V. Madge, Toughness of Bulk Metallic Glasses, Metals 5 (2015) 1279–1305.

[4]. H. X. Li, Z. C. Lu, S. L. Wang, Y. Wu, Z. P. Lu, Fe-Based Bulk Metallic Glasses Glass Formation, Fabrication, Properties and Applications, Prog. Mater. Sci. 103 (2019) 235–318.

[5]. M.E. McHenry, M.A. Willard, D.E. Laughlin, Amorphous and nanocrystalline materials for applications as soft magnets, Prog. Mater. Sci. 44 (1999) 291–433.

[6]. G. Herzer, Modern soft magnets: Amorphous and nanocrystalline materials, Acta Mater. 61 (2013) 718–734.

[7]. T. Chabi, N. Bensebaa, S. Alleg, S. Azzaza, J.J. Suñol, E.K. Hlil, Effect of the Boron Content on the Amorphization Process and Magnetic Properties of the Mechanically Alloyed $Fe_{92-x}Nb_8B_x$ Powders, J. Supercond. Nov. Magn. 32 (2019) 893–901.

[8]. F. L. Kong, C. T. Chang, A. Inoue, E. Shalaan, F. Al-Marzouki, Fe-based amorphous soft magnetic alloys with high saturation magnetization and good bending ductility, J. Alloy. Compd. 615 (2014) 163-166.

[9]. M. Ohta, Y. Yoshizawa, Cu addition effect on soft magnetic properties in Fe-Si-B alloy system, J. Appl. Phys. 103 (2008) 07E722.

[10]. Z. Li, R. Parsons, H. Kishimoto, T. Shoji, A. Kato, J. Karel, K. Suzuki, Nanocrystalline $(Fe,Co,Ni)_{86}B_{14}$ soft magnetic alloys prepared by ultra-rapid annealing, J. Alloy. Compd. 902 (2022) 162544.

[11]. E. Yuce, B. Sarac, S. Ketov, M. Reissner, J. Eckert, Effects of Ni and Co alloying on thermal, magnetic and structural properties of Fe-(Ni,Co)-P-C metallic glass ribbons, J. Alloy. Compd. 872 (2021) 159620.

[12]. S. H. Liou, S. H. Ge, J. N. Taylor, C. L. Chien, Enhanced magnetism in amorphous Fe-based alloys, J. Appl. Phys. 61 (1987) 3243.

[13]. H. Son, G. Yoo, Q. Mustaghfiroh, D.-H. Kim, H. Choi-Yim, Effect of Substituting Hf for Zr on Fe-Co-M-Nb-B (M = Zr, Hf) Amorphous Alloys with High Saturation Magnetization, Metals 12 (2022) 12.

[14]. S. Sharma, C. Suryanarayana, Effect of carbon addition on the glass-forming ability of mechanically alloyed Fe-based alloys, *J. Appl. Phys. 103 (*2008) 0135041–0135045.

[15]. A. Inoue, X. M. Wang, Bulk amorphous Fc20 (Fe-C-Si) alloys with small amounts of B and their crystallized structure and mechanical properties, Acta Mater. 48 (2000) 1383–1395.

[16]. B. L. Shen, A. Inoue, Bulk glassy Fe-Ga-P-C-B-Si alloys with high glass-forming ability, high saturation magnetization and good soft magnetic properties, Mater. Trans. 43 (2002) 1235–1239.

[17]. B. Yao, L. Si, H. Tan, Y. Zhang, Y. Li, Effects of high boron content on crystallization, forming ability and magnetic properties of amorphous $Fe_{91-x}Zr_5B_xNb_4$ alloy, J. Non-Cryst. Solids 332 (2003) 43–52.

[18]. C. Suryanarayana, Mechanical Alloying: A Novel Technique to Synthesize Advanced Materials, Research 2019 (2019) 1.

[19]. B.Avar, T. Simsek, S. Ozcan, A. K. Chattopadhyay, B. Kalkan, Structural stability of mechanically alloyed amorphous $(FeCoNi)_{70}Ti_{10}B_{20}$ under high-temperature and high-pressure, J. Alloy. Compd. 860 (2021) 158528.

[20]. J. C. de Lima, A. S. Ferreira, R. S. de Biasi, Modeling the amorphous structure of mechanically alloyed amorphous $Ni_{30}Nb_{70}$ using anomalous wide-angle X-ray scattering and reverse Monte Carlo simulations, J. Non-Cryst. Solids 447 (2016) 21–28.

[21]. M. Kunz *et al.*, A beamline for high-pressure studies at the Advanced Light Source with a superconducting bending magnet as the source, J. Synchrotron Rad. 12 (2005) 650.

[22]. C. Prescher and V. B. Prakapenka, DIOPTAS: A program for reduction of two-dimensional x-ray diffraction data and data exploration, High Press. Res. 35 (2015) 223.

[23]. A. K. Soper, Partial structure factors from disordered materials diffraction data: An approach using empirical potential structure refinement, Phys. Rev. B 72 (2005) 104204/1–104204/12.

[24]. A. K. Soper, Empirical potential Monte Carlo simulation of fluid structure, Chem. Phys., 202 (1996), 295-306.

[25]. C. Shi, O.L.G. Alderman, A. Tamalonis *et al.,* Redox-structure dependence of molten iron oxides. Commun. Mater 1 (2020) 80.

[26]. C. Y. Maghfiroh *et al,* Parameters (σ, ε) of Lennard-Jones for Fe, Ni, Pb for Potential and Cr based on Melting Point Values Using the Molecular Dynamics Method of the Lammps Program, J. Phys.: Conf. Ser. 1491 (2020) 012022.

[27]. W. Y. Ching, and C. C. Lin, Structural models for amorphous transition metal binary alloys. [Radial distribution functions, density]. United States: N. p., 1976. Web.

[28]. O. L. G. Alderman, L. B. Skinner, C. J. Benmore, A. Tamalonis, and J. K. R. Weber, Structure of Molten Titanium Dioxide, Phys. Rev. B 90 (2014) 094204.

[29]. O. Bouty, Application of the Empirical Potential Structure Refinement Technique to a Borosilicate Glass of Nuclear Interest, Procedia Materials Science 7 (2014) 32-37.

[30]. M. J. Berger, J. H. Hubbell, S. M. Seltzer, J. Chang, J. S. Coursey, R. Sukumar, D. S. Zucker, K. Olsen, XCOM: Photon Cross Section Database (version 1.5); National Institute of Standards and Technology: Gaithersburg, MD, 2010. Available online at http://physics.nist.gov/xcom.

[31]. C. N. J. Wagner, Direct methods for the determination of atomic-scale structure of amorphous solids (x-ray, electron, and neutron scattering), J. Non-Cryst. Solids 31 (1978) 1-40.

[32]. H. H. Paalman and C. J. Pings, Fourier analysis of X-Ray Diffraction Data from Liquids, Rev. Mod. Phys. 35 (1963) 389.

[33]. S. J. B. Reed, Dead time corrections for X-ray intensity measurements with a Si(Li) detector, J. Phys. E: Sci. Instrum. 5 (1972) 994.

[34]. Warren, B.F., Mozzi, R.L., Multiple Scattering of X-rays by Amorphous Samples, Acta Crys., 21 (1966) 459.

[35]. B. Kalkan, R. P. Dias, C.-S. Yoo, S. M. Clark, S. Sen, Polymorphism and pressure-induced metallization at the rigidity percolation threshold in densified $GeSe_4$ glass, J. Phys. Chem. C 118 (2014) 10.

[36]. B. Kalkan, B. Godwal, S. V. Raju, and R. Jeanloz, Local structure of molten $AuGa_2$ under pressure: Evidence for coordination change and planetary implications, Sci. Rep. 8 (2018) 6844.

[37]. T. E. Faber, J. M. Ziman, A theory of the electrical properties of liquid metals, Philos. Mag. 11 (1965) 153.

[38]. H. H. M. Balyuzi, Analytic approximation to incoherently scattered X-ray intensities, Acta Cryst. A 31 (1975) 600.

[39]. R. Babilas, Characterization of atomic-level structure in Fe-based amorphous and nano-crystalline alloy by experimental and modeling methods, Material Characterization 107 (2015) 7-13.

[40]. Y. Zhang, H. Hahn, Characterization of the free volume in a $Zr_{45.0}Cu_{39.3}Al_{7.0}Ag_{8.7}$ bulk metallic glass by reverse Monte Carlo simulation and density measurements, J. Non-Cryst. Solids 357 (2011) 1420–1425.

[41]. M.H. Cohen, D. Turnbull, On the free volume model of the liquid-glass transition, J. Chem. Phys. 52 (1970) 3038–3041.

[42]. R.B. Schwarz, R.R. Petrich, C.K. Saw, The synthesis of amorphous NiTi alloy powders by mechanical alloying, J. Non Cryst. Solids 76 (1985) 281–302.

[43]. C. C. Koch, O. B. Cavin, C. G. McKamey, et al., Preparation of amorphous $Ni_{60}Nb_{40}$ by mechanical alloying, Appl. Phys. Lett. 43 (1983) 1017.

[44]. R. W. James, Optical Principles of the Diffraction of X-rays, p.467. Cornell Unversity Press (1962).

[45] Goldman, A. (1999). Crystal Structure of Ferrites. In: Handbook of Modern Ferromagnetic Materials. The Springer International Series in Engineering and Computer Science, vol 505. Springer, Boston, MA. https://doi.org/10.1007/978-1-4615-4917-8_11.

[46] A. Hirata, Y. Hirotsu and E. Matsubara, Local Atomic Structures of Amorphous $Fe_{80}B_{20}$ and $Fe_{70}Nb_{10}B_{20}$ Alloys Studied by Electron Diffraction, Material Transactions 46 No12 (2005) 2781-2784.

[47]. J.D. Bernal, Geometry of the structure of monatomic liquids, Nature 185 (1960) 68–70.

Tables

Table 1. Lennard-Jones parameters and number of atoms used for EPSR simulations, and calculated density for $(FeCoNi)_{70}Ti_{10}B_{20}$ alloy.

Elements	**σ (Å)**	**ε (kj/mol)**	**References**	**# of atoms**
Fe	1.65	0.15	[25]	233
Co	2.61	0.50	[27]	233
Ni	1.58	0.17	[26]	233
Ti	1.31	2.23	[28]	100
B	0.85	0.25	[29]	200
Mass density: 7.06 g/cm^3				
Atomic number density (ρ_0): 0.089 atoms/Å^3				

Table 2. Cut-off distances, nearest neighbor distances and coordination numbers of the amorphous $(FeCoNi)_{70}Ti_{10}B_{20}$ obtained by constrained simulation runs.

Pairs	Cut-off distances (Å)	Interatomic distance (Å) after EP introduction	Interatomic distance (Å) before EP introduction	Coordination number
B-B	1.60	2.18	2.16	5.7
Ti-B (B-Ti)	2.00	2.46	2.44	3.8 (1.9)
Ti-Ti	2.10	2.49	2.48	4.1
Co-B (B-Co)	1.80	2.32	2.30	1.2 (1.2)
Co-Ti	2.30	2.65	2.64	0.7
Co-Co	2.00	2.53	2.53	3.8
Ni-B (B-Ni)	1.80	2.37	2.34	1.2 (1.2)
Ni-Ti	2.00	2.49	2.48	1.1

Ni-Co	2.00	2.52	2.51	3.8
Ni-Ni	2.00	2.52	2.51	3.7
Fe-B (B-Fe)	1.80	2.29	2.27	1.2 (1.2)
Fe-Ti	2.30	2.62	2.60	0.6
Fe-Co	2.00	2.49	2.48	4.0
Fe-Ni	2.00	2.53	2.52	3.6
Fe-Fe	2.00	2.51	2.49	3.9

Total coordination numbers	
Around Fe	13.3
Around Co	13.5
Around Ni	13.4
Around Ti	10.3
Around B	11.2

Figures and Figure Captions

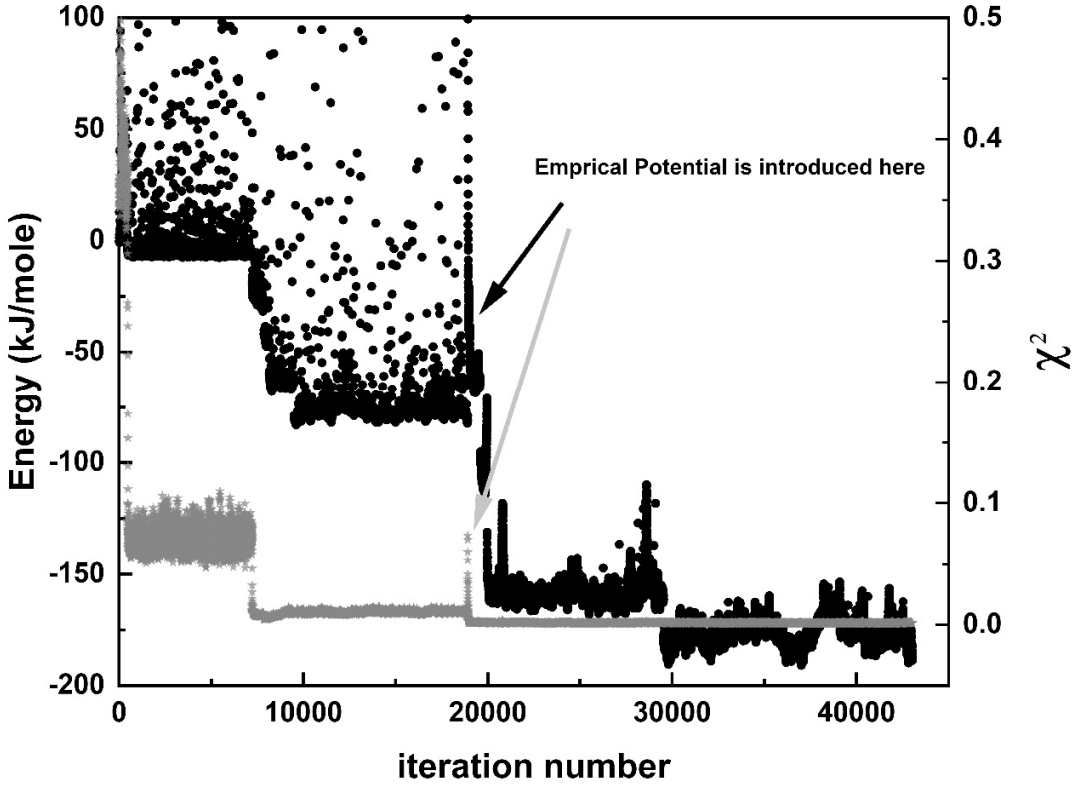

Figure 1. Energy (left panel, black dots) at each iteration of the simulation and corresponding χ^2 values (right panel, grey asterisk).

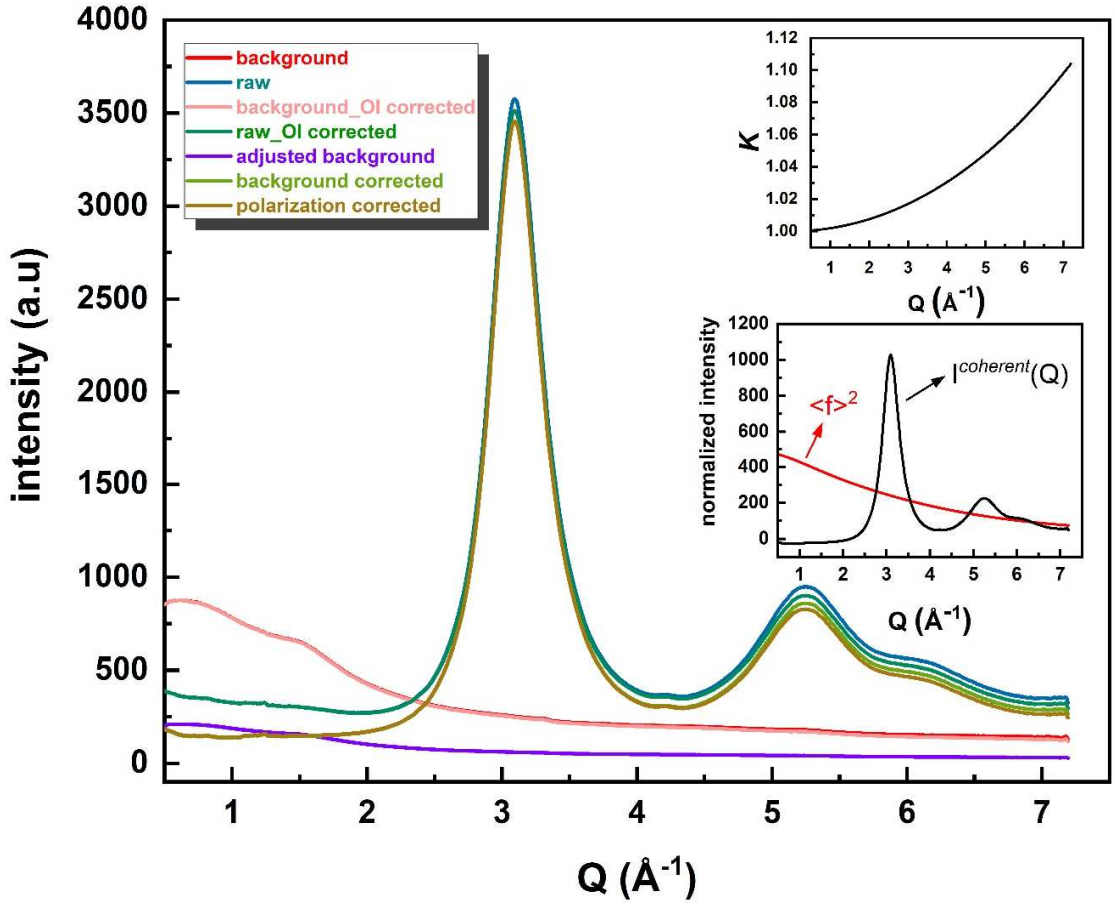

Figure 2. (Color online) Details of the data reduction process to obtain the total structure factor S(Q) from the raw diffraction data.

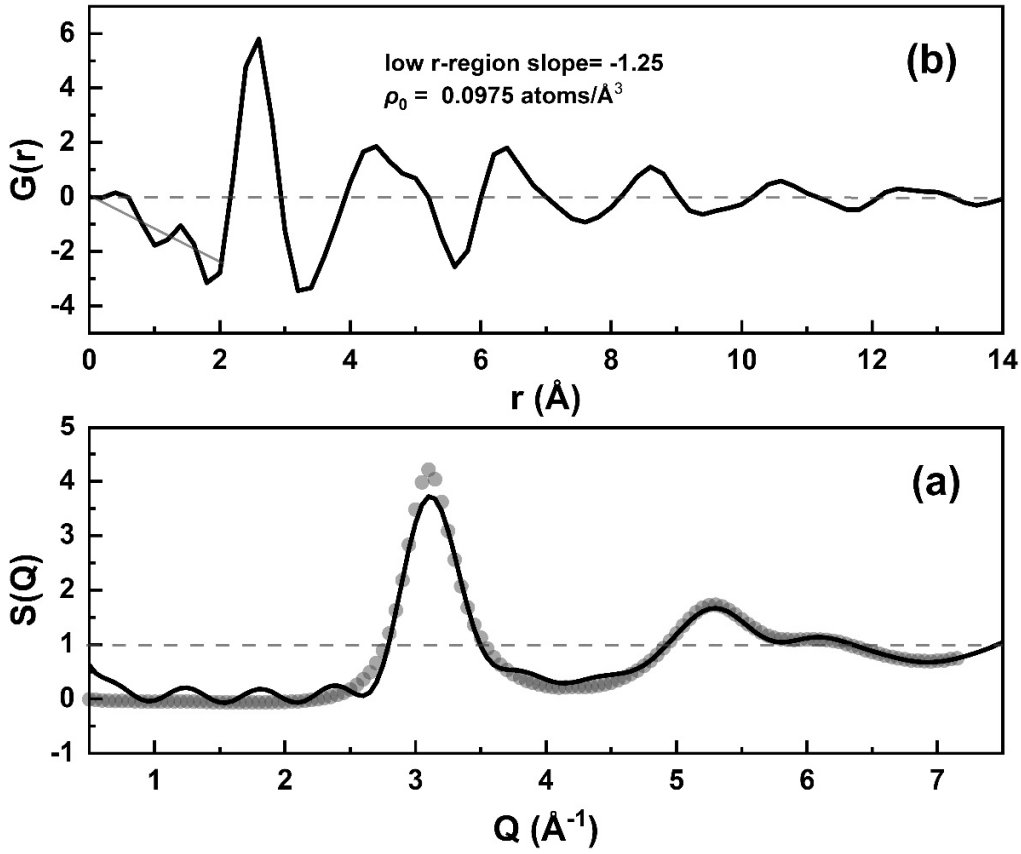

Figure 3. (a) Experimental (thick gray dots) and EPSR simulated (black line) total structure factor $S(Q)$, (b) the EPSR simulated reduced atomic pair distribution function, $G(r)$, and the linear fit below 2.0 Å giving the slope that is used to calculate the atomic number density of amorphous $(FeCoNi)_{70}Ti_{10}B_{20}$ alloy at ambient conditions.

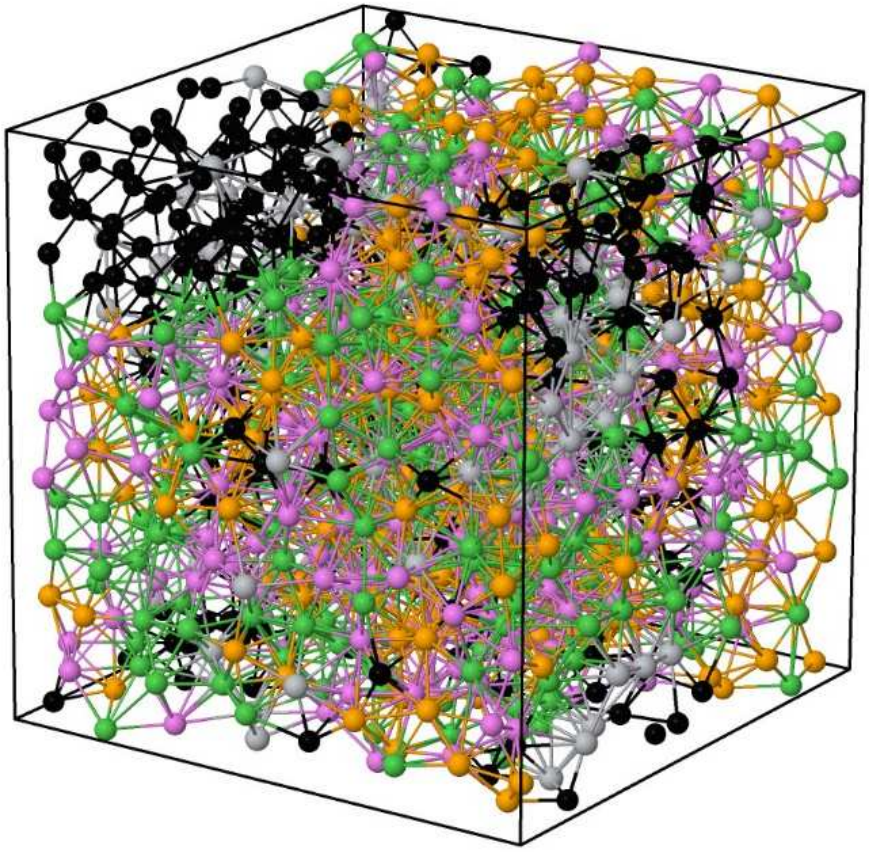

Figure 4. (Color online) 3D atomic configuration obtained from EPSR simulations, Fe: light brown, Co: pink, Ni: green, Ti: grey, and B: black balls. The length of the simulation box is 22.3 Å. (For interpretation of the colored balls in this figure, the reader is referred to the web version of this article.)

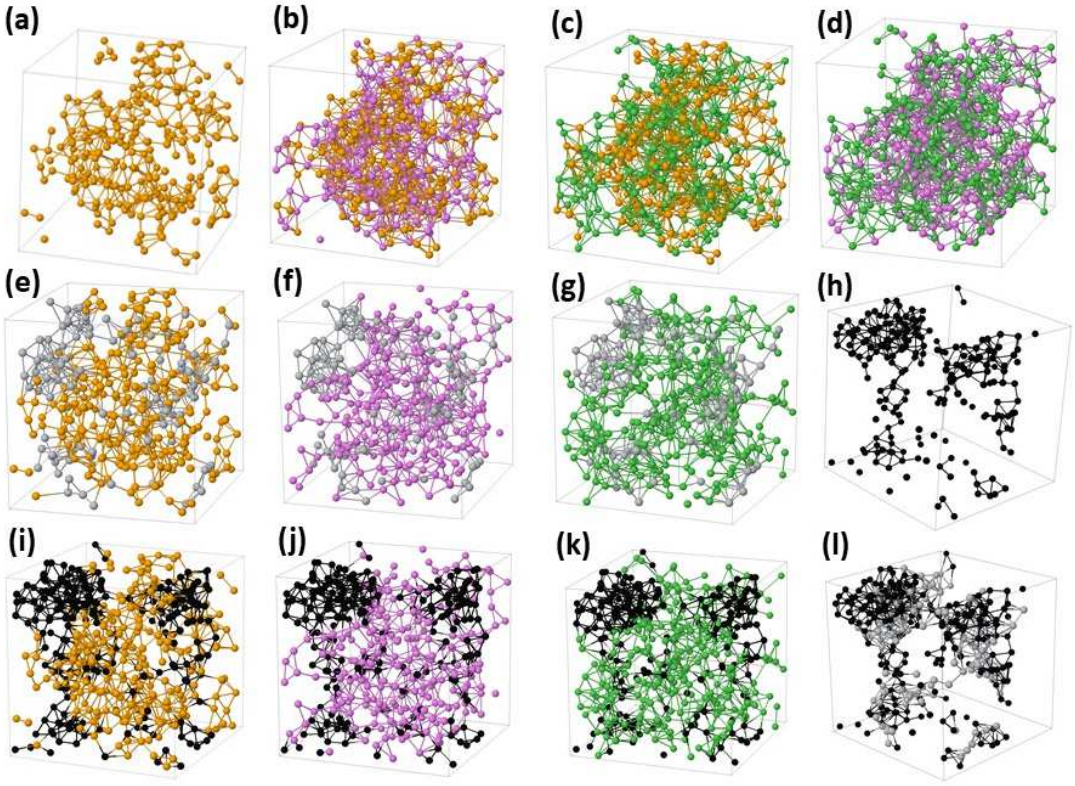

Figure 5. (Color online) The 3D atomic arrangements of (a) Fe atoms, (b) Fe and Co atoms, (c) Fe and Ni atoms, (d) Ni and Co atoms, (e) Fe and Ti atoms, (f) Co and Ti atoms, (g) Ni and Ti atoms, (h) B atoms, (i) Fe and B atoms, (j) Co and B atoms, (k) Ni and B atoms, and (l) Ti and B atoms. The atoms not displayed are excluded.

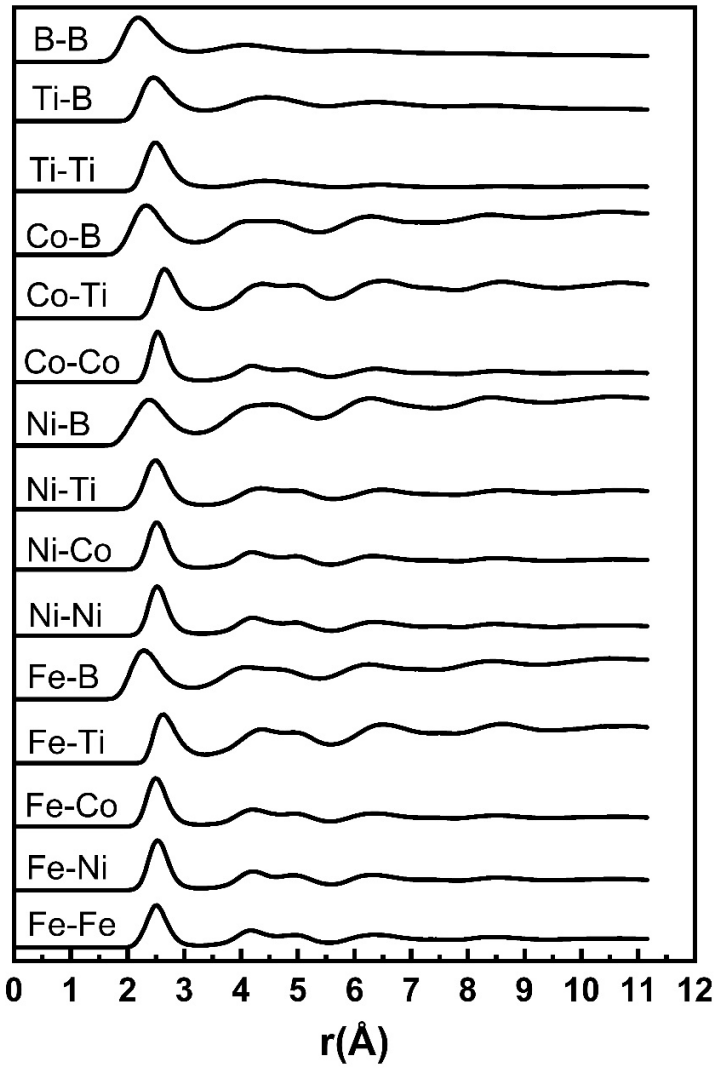

Figure 6. Partial pair distribution functions determined from EPSR simulations.

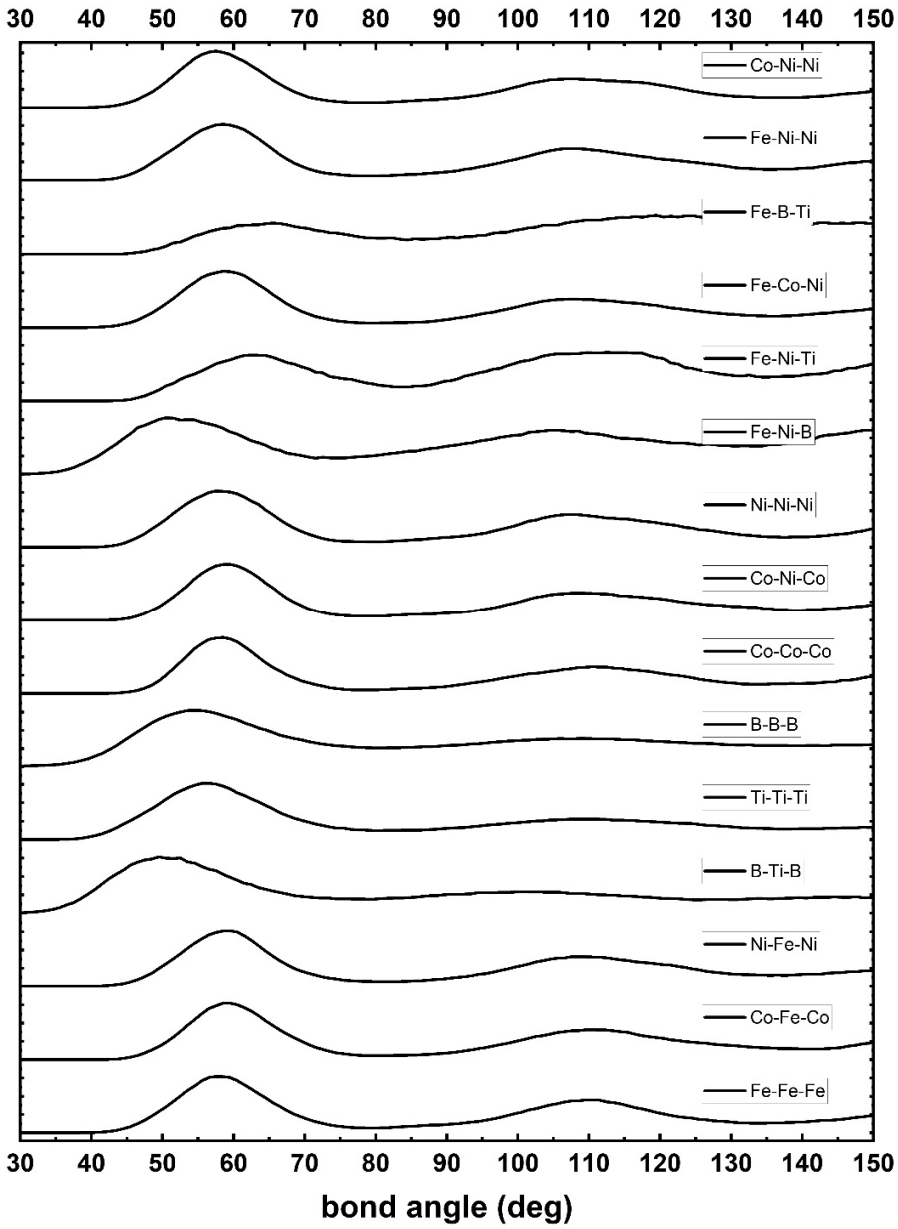
30 40 50 60 70 80 90 100 110 120 130 140 150
Co-Ni-Ni
Fe-Ni-Ni
Fe-B-Ti
Fe-Co-Ni
Fe-Ni-Ti
Fe-Ni-B
Ni-Ni-Ni
Co-Ni-Co
Co-Co-Co
B-B-B
Ti-Ti-Ti
B-Ti-B
Ni-Fe-Ni
Co-Fe-Co
Fe-Fe-Fe
30 40 50 60 70 80 90 100 110 120 130 140 150
bond angle (deg)

Figure 7. The bond-angle distributions (the angle is centered at the middle atom) obtained from the EPSR simulations.

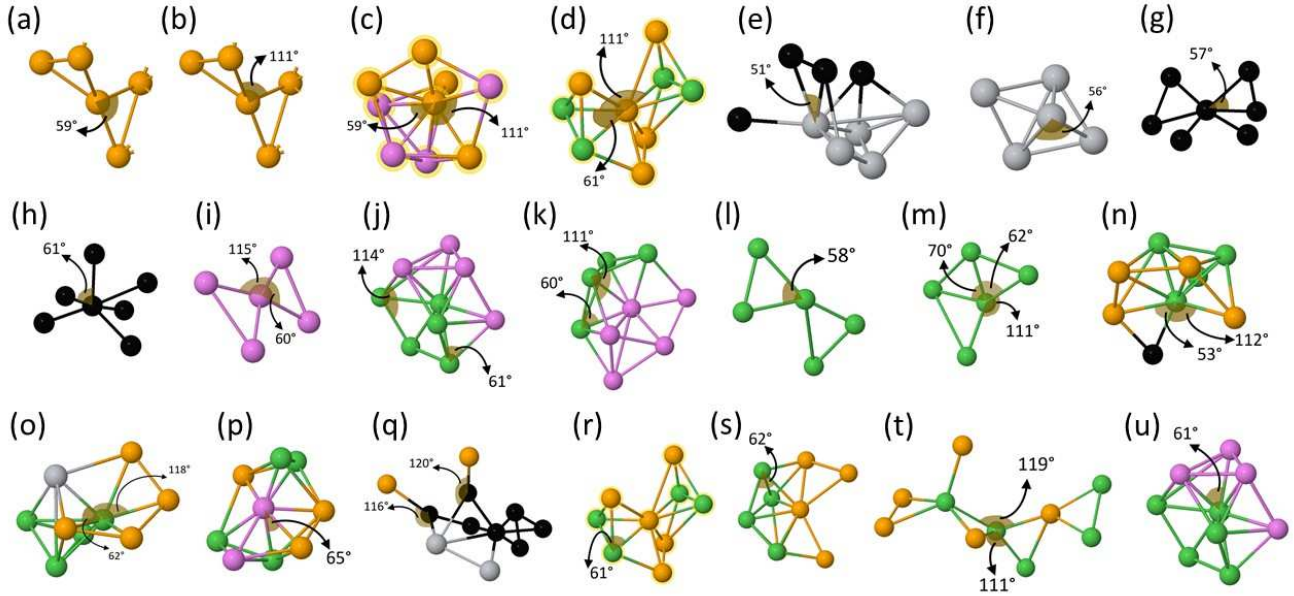

Figure 8. (Color online) The structural motifs found in $(FeCoNi)_{70}Ti_{10}B_{20}$ alloy together with bond angles describing the bond angle distribution functions presented in Figure 7. Fe: light brown, Co: pink, Ni: green, Ti: grey, and B: black balls.